Noname manuscript No.
(will be inserted by the editor)

On the loss of symmetry in toughness dominated hydraulic fractures

Erwan Tanné · Blaise Bourdin · Keita Yoshioka

Received: date / Accepted: date

Abstract Fracking, or hydraulic fracturing, is a ubiquitous technique for generating fracture networks in rocks for enhanced geothermal systems or hydrocarbon extraction from shales. For decades, models, numerical simulation tools, and practical guidelines have been based on the assumption that this process generates networks of self-similar parallel cracks. Yet, some field and laboratory observations show asymmetric crack growth, and material heterogeneity is routinely attributed for it. Here, we show that simultaneous growth of multiple parallel cracks is impossible and that a single crack typically propagates asymmetrically in toughness dominated hydraulic fracturing, in which viscous dissipation of the fluid is negligible. In other words, loss of symmetry is a fundamental feature of hydraulic fracturing in a toughness dominated regime and not necessary the result of material heterogeneities. Our findings challenge the assumptions of symmetrical growth of hydraulic fractures commonly made in practice, and point to yet another instability other than material heterogeneity.

Keywords Hydraulic fracturing · Loss of symmetry · Phase-field models of fracture · Gradient damage models

Erwan Tanné
ENSTA Bretagne, IRDL UMR 6027 CNRS, 2 rue François Verny, 29806 Brest cedex 9, France
E-mail: erwan.tanne@gmail.com

Blaise Bourdin
Department of Mathematics, Louisiana State University, Baton Rouge LA 70803, USA *Present address:* Department of Mathematics & Statistics, McMaster University, 1280 Main Street West, Hamilton ON L8S 4K1, Canada
E-mail: bourdin@mcmaster.ca

Keita Yoshioka
Department of Environmental Informatics, Helmholtz Centre for Environmental Research – UFZ, Permoserstrasse 15, 04318 Leipzig, Germany
Department of Civil Engineering, University of Manitoba, 15 Gilson Stree, Winnipeg, MB R3T 5V6, Canada
E-mail: keita.yoshioka@ufz.de

1 Introduction

Starting with the work of Sneddon and Elliott [33], the problem of a penny-shaped hydraulic fracture subjected to a uniform pressure field has been studied in depth. The symmetries of the elastic fields have been leveraged to study its propagation, as reviewed in [16] and references within. When multiple hydraulic cracks are involved, many existing models are limited to planar geometries [28, 24] or other restrictions such as non intersecting or non-branching cracks [40, 42, 14, 10, 22, 32]. These geometric restrictions are often deemed acceptable, arguing that the symmetry of the problem (rotational and translational in the case of an infinite array of cracks) will translate into that of the solution. Yet, Gao and Rice [21] have computed the stress intensity factors for a penny-shaped crack under uniaxial tensile loads and shown that shape instabilities will arise even in an isotropic homogeneous infinite medium. Complex non-symmetric fracture patterns have been observed in field operations by monitoring microseismic [37, 19, 13]. For example, during a hydraulic fracturing operation in a horizontal well with multiple mass injection points, the microseismic activities indicate non-symmetric fracture propagation at the expense of others (see Fig. 1(a)), a phenomenon often attributed to heterogeneities. Furthermore, non-circular fracture patterns in isotropic homogeneous materials observed in experiments (see Fig. 1(b-c)) are not fully explained. In this context, it is natural to challenge the statement that loss of symmetry in hydraulic fracturing is solely due to materials heterogeneities.

In what follows, we study the most idealized setting, often referred to as toughness dominated, of an incompressible and inviscid fluid injected in a network of (hydraulically) connected equidistant parallel cracks in an impermeable isotropic homogeneous infinite medium. In two space dimension, we perform a stability analysis to show that even in the case of far apart cracks, a single crack will always dominate, and that simultaneous propagation of an array of identical cracks is actually the *least* stable configuration. Numerical simulations suggest that this is still the case when crack interactions are accounted for.

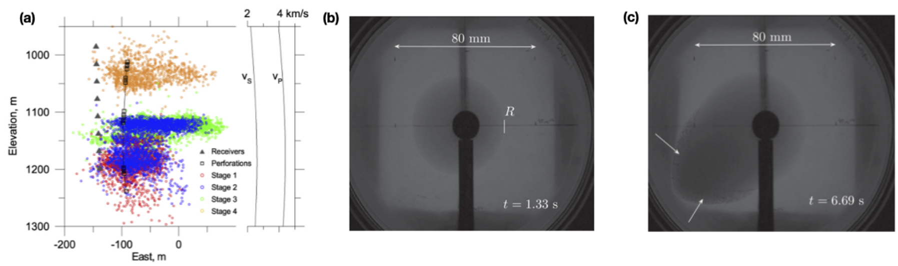

Fig. 1 (a) A top view of microseismic activities during the multi–stage hydraulic fracturing operation in a horizontal well. Microseismic activities indicate asymmetric hydraulic fracture growth out of the perforations [19]. (b,c) Hydraulic-fracture laboratory experiment showing how a penny-shape crack can evolve off-centered even in a synthetic homogeneous material [8].

2 Classical analysis of a pressurized crack in an infinite domain

2.1 Non-interacting single crack

Consider a straight crack of length $2l_0$, $\Gamma = (-l_0, l_0) \times \{0\}$, in an infinite two dimensional (2D) domain occupied by a homogeneous isotropic perfectly brittle material with Young's modulus E, Poisson ratio ν, and critical elastic energy release rate G_c. Assuming a uniform pressure p acting on both crack lips, the elastic energy becomes [33,3]

$$\mathcal{E}_V(l_0) := \frac{E'V^2}{4\pi l_0^2},$$

where $E' = E$ in plane stress condition and $E' = E/(1-\nu^2)$ in plane strain. The elastic energy release rate *with respect to a volume change* is

$$G_V(l_0) = -\frac{1}{2}\frac{\mathrm{d}\mathcal{E}_V}{\mathrm{d}l_0}(l_0) = \frac{E'V^2}{4\pi l_0^3}. \tag{1}$$

Assuming a quasi-static evolution driven by an increasing injection volume, we have that $G_V(l_0) \leq G_c$ as long as

$$V \leq V_c(l_0) := 2\left(\frac{\pi G_c l_0^3}{E'}\right)^{1/2},$$

at which point the pressure reaches the critical value

$$p_c(l_0) := \left(\frac{G_c E'}{\pi l_0}\right)^{1/2}.$$

2.2 Non-interacting multiple cracks

Consider now N straight cracks of length $(l_1, l_2, \dots, l_N)$ hydraulically connected (*e.g.* through a wellbore) so that the fluid pressure in all cracks is p but distant enough so that we can neglect the influence of each crack on the elastic field and energy release rate of the others. Let $V = \sum_{i=1}^N V_i$ be the total injection volume. From the single crack analysis, we have $V_i = 2\pi p l_i^2/E'$ so that

$$p = \frac{VE'}{2\pi \sum_{j=1}^N l_j^2}$$

Then the elastic energy of the system for a given injected pressure is:

$$\mathcal{E}_V(l_1, \dots l_N) = \frac{1}{2}pV = \frac{E'}{4\pi}\frac{V^2}{\sum_{j=1}^N l_j^2}.$$

Let $G_V(l_1, \dots l_N)[\delta l_1, \dots, \delta l_N]$ be the elastic energy release rate associated with a crack increment vector $\langle \delta l_1, \dots, \delta l_N \rangle$, obtained by taking the directional derivative of $\mathcal{E}_V$ at $(l_1, \dots l_N)$ in the direction $\langle \delta l_1, \dots, \delta l_N \rangle$. Recalling that $\mathcal{E}_V(l_1, \dots l_N)$

denotes the elastic energy associated with N cracks of length $(2l_1, \dots 2l_N)$, we have

$$\begin{aligned} G_V(l_1, \dots l_N) \cdot \langle \delta l_1, \dots, \delta l_N \rangle &:= -\frac{1}{2} \nabla \mathcal{E}_V(l_1, \dots l_N) \cdot \langle \delta l_1, \dots, \delta l_N \rangle \\ &= \frac{E' V^2}{4\pi \left(\sum_{j=1}^N l_j^2 \right)^2} \sum_{p=1}^N l_p \delta l_p. \end{aligned}$$

i.e.

$$G_V(l_1, \dots l_N) = \frac{E' V^2}{4\pi \left(\sum_{j=1}^N l_j^2 \right)^2} \cdot \langle l_1, \dots, l_N \rangle .$$

Suppose first that the l_i are not all equal, and let l_q be the longest of the cracks. Then, amongst all crack increments $\langle \delta l_1, \dots, \delta l_N \rangle$ such that $\sum_{j=1}^N \delta l_j = \delta l$, G_V is maximized by the configuration $\delta l_q = \delta l$ and $\delta l_i = 0$, $i \neq q$, *i.e.* Griffith criticality will first be attained by growing only the longest crack. Since $p_c(l)$ is a decreasing function, the same scenario will repeat itself and the longest crack will continue to grow while all others will remain sub-critical.

When all cracks are of equal length, let $l := l_1 = \dots = l_N$. We have that

$$G_V(l, \dots, l) \cdot \langle \delta l_1, \dots, \delta l_N \rangle = \frac{E' V^2}{4\pi N^2 l^3} \sum_{p=1}^N \delta l_p = \frac{E' V^2 \delta l}{4\pi N^2 l^3}.$$

To determine the crack increment with the largest energy release, we study the eigenvalues of the Hessian matrix of the elastic energy $\mathcal{E}_V$ with respect to variations of crack length for fixed injected volume, *i.e.* by computing the gradient DG_V of the elastic energy release rate:

$$DG_V(l, \dots l) = \frac{E' V^2}{4\pi N^2 l^4} \left(\mathbf{I} - \frac{4}{N} \mathbb{1} \otimes \mathbb{1} \right),$$

where $\mathbf{I}$ denotes the identity matrix in dimension N and $\mathbb{1} := \langle 1, \dots, 1 \rangle$. Using the identity $\det(\mathbf{I} + \mathbf{c} \otimes \mathbf{d}) = 1 + \mathbf{c} \cdot \mathbf{d}$ for any $\mathbf{c}, \mathbf{d} \in \mathbb{R}^N$ [29] (p. 475), we obtain that the eigenvalues of $DG_V(l, \dots l)$ are $\lambda_1 = \dfrac{-3E' V^2}{4\pi N^2 l^4}$ with multiplicity 1 and $\lambda_2 = \dots = \lambda_N = \dfrac{E' V^2}{4\pi N^2 l^4}$ with multiplicity $N-1$. The eigenvector for the negative eigenvalue λ_1 is $v_1 = \mathbb{1}$ while those associated with the positive eigenvalues are $v_i = e_1 - e_j$, $j = 2, \dots, N$, e_i, $i = 1, \dots, N$ being the vectors of the canonical basis of $\mathbb{R}^N$. Note that v_1, the eigenvector associated with equal growth of all cracks, *minimizes* the elastic energy release rate and

$$DG(l, \dots, l) \mathbb{1} \cdot \mathbb{1} = \frac{-3E' V^2}{4N^2 \pi l^4}.$$

In other words, in the limit of non-interacting cracks with equal length, symmetric growth of all crack satisfies Griffith's criterion (formally $G = G_c$) but it is the *worst* configuration from an energetic viewpoint.

The other eigenvectors do not correspond to admissible perturbations. Maximizers of the elastic energy release rate of the form $\delta l e_j$, $j = 1, \ldots, N$ are obtained by projecting them onto the cone of admissible perturbations, and

$$DG(l, \ldots, l)e_j \cdot e_j = \frac{E'V^2}{4N^2\pi l^4}\left(1 - \frac{4}{N}\right).$$

Stable configurations satisfying Griffith criterion consist therefore in growing a single arbitrary crack.

The same argument can be extended to an infinite network of "far enough" parallel aligned cracks where a superposition principle can be used to show that the elastic energy of a network of equi-distributed cracks of equal length under equal pressure is the sum of the elastic energy of each crack pressurized separately. It also extends trivially to the three-dimensional (3D) case. Of course, the possibility remains that interactions between "close enough" cracks plays a stabilizing role that can lead to simultaneous propagation. We used numerical simulations to show that this is not the case.

3 A variational phase-field model for pressurized fractures

3.1 A variational approach to the propagation of pressurized cracks under prescribed injection volume

In the toughness dominated regime of hydraulic fracturing [17], the injected fluid can be regarded as inviscid, incompressible and the leak-off is negligible, so that we are not concerned with poro-elastic effects. Following the now classical work of Francfort and Marigo [20], Griffith's criterion [23] can be formulated as a variational principle. Consider a domain $\Omega \subset \mathbb{R}^N$, $N = 2$ or 3 in its reference configuration occupied by a perfectly brittle material with Hooke's law $\mathtt{A}$ and critical energy release rate G_c. Let $\Gamma \subset \Omega$ with $\Gamma \cap \partial\Omega = \emptyset$ denote a regular enough crack set with normal vector ν_Γ providing an orientation from the side Γ^- to Γ^+. The sound region $\Omega \setminus \Gamma$ is subject to a time independent boundary displacement $\bar{\mathbf{u}}(t) = 0$ on the Dirichlet part of its boundary $\partial_D\Omega$ while the remaining part $\partial_N\Omega = \partial\Omega \setminus \partial_D\Omega$ remains traction-free. Following Francfort and Marigo's variational approach to fracture [20, 5], the total energy associated to a configuration $(\mathbf{u}, \Gamma)$ is

$$\mathcal{E}(\mathbf{u}, \Gamma) := \int_{\Omega\setminus\Gamma} \frac{1}{2}\mathtt{A}\,\mathrm{e}(\mathbf{u}) \cdot \mathrm{e}(\mathbf{u})\,\mathrm{d}x + G_c\mathcal{H}^{N-1}(\Gamma), \tag{2}$$

where $\mathcal{H}^{N-1}$ denotes the $N-1$–dimensional Hausdorff measure, *i.e.* $\mathcal{H}^{N-1}(\Gamma)$ is the aggregate length of the unknown fracture set Γ in 2D and its surface area in 3D.

The total volume of the cavity formed by the crack Γ in the deformed configuration is

$$V(\mathbf{u}) := \int_\Gamma \left(\mathbf{u}^+ - \mathbf{u}^-\right) \cdot \nu_\Gamma \, d\mathcal{H}^{N-1},$$

where $\mathbf{u}^+$ and $\mathbf{u}^-$ represent the one-sided traces of $\mathbf{u}$ along Γ^+ and Γ^- respectively. Given a discrete set of time steps $0 = t_0 < t_1 < \cdots < t_m = T$ and injection volumes $V_1, \dots V_m$, we seek configurations $(\mathbf{u}_i, \Gamma_i)$ minimizing $\mathcal{E}$ amongst all kinematically admissible displacement fields $\mathbf{u}$ such that $V(\mathbf{u}) = V_i$ and all crack sets Γ satisfying a growth condition $\Gamma_j \subset \Gamma_i$ for all $j < i$, with Γ_0 representing pre-existing cracks if any. It is worth emphasizing that the model makes no assumptions on the crack geometry Γ_i besides the irreversibility condition. Instead, the crack geometry is fully determined by the successive minimization of the total energy (2).

Let $\mathcal{L}(\mathbf{u}, \Gamma, q) := \mathcal{E}(\mathbf{u}, \Gamma) - q\,(V(\mathbf{u}) - V_i)$ be the Lagrangian associated with this constrained minimization problem (ignoring the growth constraint for the sake of simplicity), q denoting the Lagrange multiplier associated with the volume constraint. Stability with respect to q gives the volume constraint, and stability with respect to $\mathbf{u}$, considering an admissible perturbation $\mathbf{v} \in H^1(\Omega \setminus \Gamma; \mathbb{R}^N)$ vanishing on $\partial_D \Omega$ gives

$$\langle \mathcal{L}_{\mathbf{u}}(\mathbf{u}, \Gamma, q), \mathbf{v} \rangle = \int_{\Omega \setminus \Gamma} \mathtt{A}\, \mathrm{e}(\mathbf{u}) \cdot \mathrm{e}(\mathbf{v})\, \mathrm{d}x - q \int_{\Gamma} \left(\mathbf{v}^+ - \mathbf{v}^- \right) \cdot \nu_\Gamma d\mathcal{H}^{N-1} = 0.$$

Using Green's formula on $\Omega \setminus \Gamma$, we get

$$\begin{aligned} -\int_{\Omega\setminus\Gamma} \mathrm{div}\,(\mathtt{A}\,\mathrm{e}(\mathbf{u})) \cdot \mathbf{v}\, \mathrm{d}x + \int_{\partial\Omega} \mathtt{A}\,\mathrm{e}(\mathbf{u})\nu_\Omega \cdot \mathbf{v}\, d\mathcal{H}^{N-1} \\ + \int_{\Gamma^+} \mathtt{A}\,\mathrm{e}(\mathbf{u})(-\nu_\Gamma) \cdot \mathbf{v}\, d\mathcal{H}^{N-1} + \int_{\Gamma^-} \mathtt{A}\,\mathrm{e}(\mathbf{u})\nu_\Gamma \cdot \mathbf{v}\, d\mathcal{H}^{N-1} \\ - q \int_{\Gamma^+} \mathbf{v}^+ \cdot \nu_\Gamma\, d\mathcal{H}^{N-1} + q \int_{\Gamma^-} \mathbf{v}^- \cdot \nu_\Gamma\, d\mathcal{H}^{N-1} = 0, \end{aligned}$$

ν_Ω denoting the outer normal vector to Ω. From the arbitrariness of $\mathbf{v}$, we recover the equations of linearized elasticity where the Lagrange multiplier q can be interpreted as the injection pressure p:

$$\begin{aligned} -\mathrm{div}\sigma &= 0 && \text{in } \Omega \setminus \Gamma, \\ \sigma\nu_\Omega &= 0 && \text{on } \partial\Omega, \\ \sigma\nu_\Gamma &= -p\nu_\Gamma && \text{on } \Gamma^\pm, \end{aligned}$$

with $\sigma = \mathtt{A}\,\mathrm{e}(\mathbf{u})$.

Note that from Clapeyron's formula, we get that if $\mathbf{u}$ minimizes (2) and p is the Lagrange multiplier associated with the volume constraint V, one has that

$$\int_{\Omega\setminus\Gamma} \mathtt{A}\,\mathrm{e}(\mathbf{u}) \cdot \mathrm{e}(\mathbf{u})\, \mathrm{d}x = p \int_\Gamma \left(\mathbf{u}^+ - \mathbf{u}^- \right) \cdot \nu_\Gamma\, d\mathcal{H}^{N-1} = pV,$$

so that

$$\mathcal{E}(\mathbf{u}, \Gamma, V) = \frac{1}{2} pV + G_c \mathcal{H}^{N-1}(\Gamma).$$

3.2 Variational phase-field approximation

The main difficulty in numerical implementation of (2) is to handle discontinuous displacements along unknown surfaces. Variational phase-field models, originally devised in image reconstruction and extended to brittle fracture [4,5], have become increasingly popular due to their ability to handle arbitrary crack geometries in 2D and 3D on a fixed mesh.

We follow this approach by introducing a regularization length ℓ, an auxiliary field α with values in $[0,1]$ representing the unknown crack surface, and the regularized energy

$$\mathcal{E}_\ell(\mathbf{u},\alpha) = \int_\Omega \frac{1}{2}(1-\alpha)^2 \mathtt{A}\,\mathrm{e}(\mathbf{u})\cdot\mathrm{e}(\mathbf{u})\,\mathrm{d}x + \frac{3G_\mathrm{c}}{8}\int_\Omega \frac{\alpha}{\ell} + \ell|\nabla\alpha|^2\,\mathrm{d}x, \quad (3)$$

where $\alpha = 0$ corresponds to the undamaged state of material while cracks are represented by smooth transition from 0 to 1 and back to 0 concentrated on regions of width $\mathcal{O}(\ell)$. Note that (3) (often referred to as AT_1) is slightly different from the regularization proposed in [3] (AT_2). This regularization has been shown to capture crack nucleation more accurately [31,27,35]. In order to account for the volume constraint, we follow the approach of [3,12], and notice that the total aperture $V(\mathbf{u})$ (hence the work of the pressure force) can be approximated by

$$V_\ell(\mathbf{u},\alpha) = -\int_\Omega \mathbf{u}\cdot\nabla\alpha\,\mathrm{d}x.$$

At each time step, the constrained minimization of the fracture energy $\mathcal{E}$ is then replaced with that of $\mathcal{E}_\ell$, with respect to all $(\mathbf{u}_i,\alpha_i)$ such that $\mathbf{u}_i$ is kinematically admissible, satisfies the regularized volume constraint $V_\ell(\mathbf{u}_i,\alpha) = V_i$ and the crack growth constraint $0 \le \alpha_{i-1} \le \alpha_i \le 1$.

As $\ell \to 0$, classical approximation results can be extended to show the Γ-convergence of (3) to (2) [5]. This result provides the basic rationale for the phase-field approximation, *i.e.* that the minimizers of $\mathcal{E}_\ell$ converge to that of $\mathcal{E}$ as $\ell \to 0$. Typically, one focuses on the minimization of $\mathcal{E}_\ell$ for a given fixed but "small" ℓ, noticing that such problem only involves smooth (H^1) functions that can be properly approximated by conventional finite elements on a fixed mesh, for instance.

3.3 Numerical implementation

We can extend the alternate minimization algorithm [4] to volume-constrained minimization [3]. Energy minimization with respect to the displacement field under a volume constraint can be achieved in two steps: compute the elastic displacement associated with a unit pressure p for a given phase-field variable (or crack geometry) then compute the value of the pressure for which the target volume is attained (*i.e.* the Lagrange multiplier associated with the volume constraint.) which is a simple rescaling for linear elastic materials. Our minimization algorithm is given in Algorithm 1, where δ_α is a fixed tolerance and $k_{\max}$ a large parameter aimed at preventing endless iteration should the algorithm diverge.

Here we are not concerned with unilateral contact (material interpenetration), so that minimization of the total energy with respect to the displacement is a simple linear problem whose solution depends linearly on the constant pressure field. Hence, the mapping between injected volume and injection pressure (for a given α) is linear so that p_i^{k+1} can be computed explicitly.

Algorithm 1 Volume driven hydraulic fracturing algorithm

1: Let $\alpha_{-1} = 0$ (or construct a phase field compatible with initial cracks)
2: **for** $i = 1$ to m **do**
3: $k \leftarrow 1$, $\alpha_i^0 = \alpha_{i-1}$
4: **repeat**
5: Compute the displacement with $p = 1$:

$$v_i^{k+1} \leftarrow \operatorname*{argmin}_{u \in \mathcal{C}_i} \left\{ \mathcal{E}_\ell(u, \alpha_i^k);\ p = 1 \right\}$$

6: Compute the crack pressure

$$p_i^{k+1} \leftarrow \frac{V_i}{-\int_\Omega v_i^{k+1} \cdot \alpha_i^k \, dx} v_i^{k+1}$$

7: Scale the displacement with the volume constraint

$$u_i^{k+1} \leftarrow p_i^{k+1} v_i^{k+1}$$

8: Minimize the total energy with respect to α

$$\alpha_i^{k+1} \leftarrow \operatorname*{argmin}_{\alpha \geq \alpha_{i-1}} \left\{ \mathcal{E}_\ell(u^{k+1}, \alpha);\ p = p_i^{k+1} \right\}$$

9: **until** $\left| \alpha_i^{k+1} - \alpha_i^k \right|_{L^\infty} \leq \delta_\alpha$ or $k = k_{\max}$
10: $u_i \leftarrow u_i^{k+1}$
11: $\alpha_i \leftarrow \alpha_i^{k+1}$

4 Variational analysis of multi-fracturing

4.1 Interacting cracks

Consider an infinite network of evenly distributed, aligned, parallel cracks with length $2l$ and spacing 2δ (see Fig. 2) subject to a given pressure p. The volume of each crack is [34]

$$V_p(\rho) = \frac{8p\delta^2}{E'} \rho^2 f(\rho),$$

where $\rho = l\pi/2\delta$ and[1] $f(\rho) = 1/\sqrt{1+\rho^2}$. The pressure that meets the Griffith criterion is

$$p(\rho) = \sqrt{\frac{E' G_c}{\delta \left(\rho^2 f(\rho) \right)'}}.$$

[1] The expression from [34] is $f(\rho) = 1 - \rho^2/2 + \rho^4/3 + o(\rho^6)$, whereas [30] gives $f(\rho) = 1 - \rho^2/2 + 3\rho^4/8 + o(\rho^6)$ which is the first terms of the McLaurin series of $1/\sqrt{1+\rho^2}$.

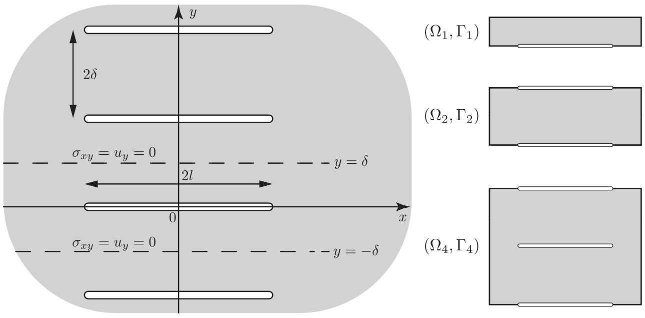

Fig. 2 (left): infinite network of cracks studied in [34], (right) decomposition in periodicity cell of increasing size.

We performed a series of numerical simulations using a variational phase-field model [2] on sub-domains of width $2L$ with initial cracks of length $2l_0$ containing n initial cracks ($n = 1, 2, 4, 6$) denoted by Ω_1, Ω_2, Ω_4, and Ω_6 respectively (Fig. 2). This numerical approach does not assume any a priori hypotheses on the crack path [4, 5] so that any number of crack can grow in any direction in our simulations. The prescribed displacements on the top and bottom boundaries are $u_y(0) = u_y(n\delta) = 0$ and $u_x(\pm L) = 0$ on the sides, so that we can view these domains as periodicity cells of an infinite network of cracks. We rewrite the energy in non-dimensional form by rescaling the displacements by a factor $\sqrt{E'/G_c}$, and the pressure by $1/\sqrt{G_c E'}$, so that in our computations, we can use unit Young's modulus and fracture toughness. The parameters used in the computations are (in non-dimensional form) $L = 10$, $\delta = 1$, $l_0 = 0.115$, and $\nu = 0$. The choice of a zero Poisson ratio is dictated by numerical convenience. Because the main driver in the development of instabilities in the crack length is the convexity of the total energy with respect to individual crack length, this choice does not impact the qualitative behavior illustrated below. The mesh size and regularization parameter in the simulations (see Appendix) are $h = 0.005$ and $\ell = 3h$. Using symmetries and translations, we can reconstruct periodic solutions for the infinite domain problem (see Fig 3). In all cases, a single crack propagates, which is consistent with the previous analysis.

Figure 4 (top-left) compares the normalized pressure and a total energy "density" defined as $\mathcal{E}_n := \left(\frac{1}{2}pV + G_c l\right)/n$ (using (3.1)) against the closed form solution given earlier. As expected, until the onset of propagation, all cases behave identically. Simulation on Ω_1 (corresponding to all cracks propagating) closely matches the theoretical pressure and total energy but larger computational domains lead to a larger pressure drop and lower total energy. When the computational domain is interpreted as a periodicity cell of growing size, the total energy of the system decreases when the number of growing cracks decreases. Again, this lends credentials to our claim that growth of a single crack is always the state of least total energy (*i.e.* is the most stable state) associated with the largest injection pressure drop. This behavior is further quantified in Fig. 4 (bottom). The solid lines show the the computed critical pressure normalized by $p_c(l_0)$ from [34] against the crack density (or spacing $1/\rho$ to be precise). The dashed lines are the ratio $r_p(\rho) := p(\rho)/p_c(l)$, the closed form critical propagation pressure in an array of crack of density ρ over that of a single crack of the same length, whose density

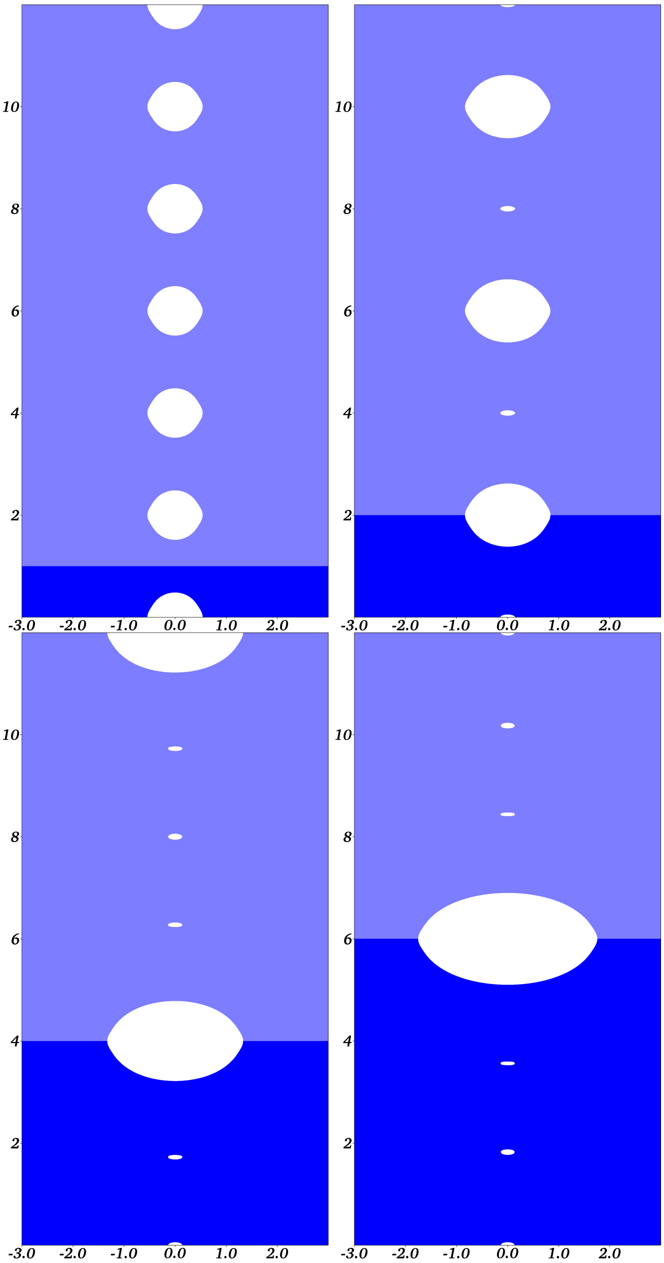

Fig. 3 Domains in the deformed configuration (deformation magnified) for Ω_1 (top-left), Ω_2 (top-right), Ω_4 (bottom-left) and Ω_6 (bottom-right). The fractured material corresponding to α close to 1 is removed for visualization purpose. The color-saturated region in the bottom of each picture is the computational domain. A succession of mirror symmetries and translations can map the computational domain into an infinite vertical strip of width $2L$.

is replaced with the "effective" density ρ/n, which reads

$$r_p = \sqrt{\frac{2((\rho/n)^2+1)^{3/2}}{(\rho/n)^2+2}}.$$

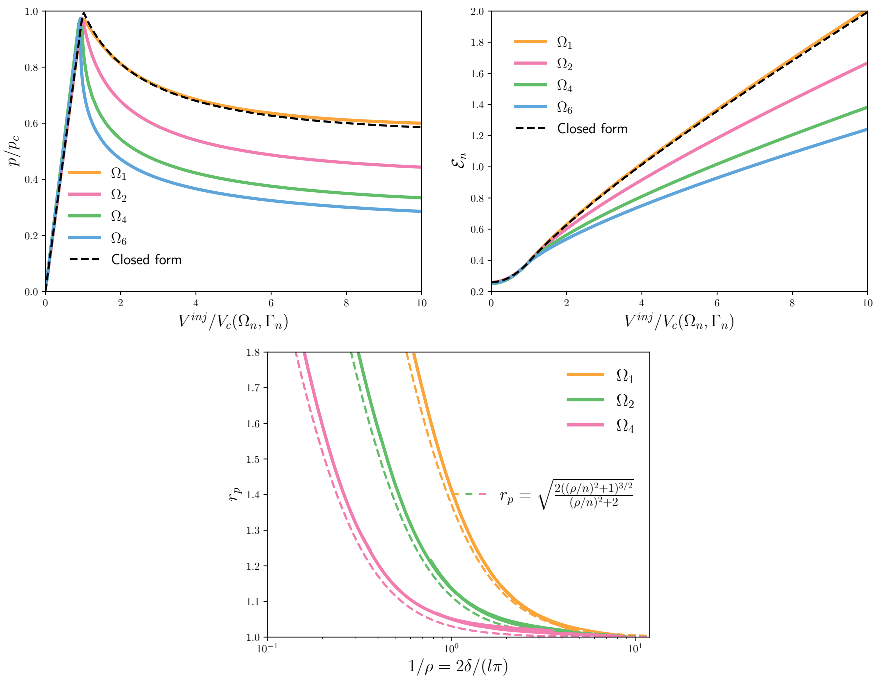

Fig. 4 Normalized pressure (top-left) and the energy density (top-right) vs. injected volume in numerical simulations (solid lines) compared to the closed form solution (dashed lines). (bottom) Ratio of critical pressures (multi-fracturing over single fracture) vs. the inverse of the fracture density in numerical simulations (solid lines) compared to $r_p(\rho/n)$ (dashed lines).

As the initial cracks spacing increases, all curves coalesce and all these cases become equivalent. For a given spacing δ or density ρ, the critical pressure decrease when the size of the periodicity cell n increases, and the ratio approaches 1. In other words, given any density of initial cracks, one and only one of the initial cracks will start propagating at the critical pressure $p_c(l_0)$. In a system consisting of a finite number of equi-distributed cracks, the same analysis implies that a single crack will grow at a critical pressure that is strictly greater than $p_c(l_0)$. Our simulation shows that the critical pressure ratio is very close to the analytic expression $r_p(\rho/n)$. As in the case of non-interacting cracks, an analysis based on Griffith criterion [34] gives a good estimate of the critical propagation pressure, but fails to identify the proper propagation pattern.

4.2 Interacting dense cracks

For closely packed initial cracks, the difference becomes even more striking. Figure 5 (top) shows 2D simulations with $\delta = 2l_0$ in the configuration Ω_2 and Ω_4. Again, a single crack grows in all cases with the notable difference that only one tip of one crack propagates, breaking the mirror symmetry of the solution. Similarly, a 3D simulation in the Ω_2 configuration (Figure 5 (bottom)) shows that a single crack grows into a non axially symmetric egg shape, which is consistent with the observations in Figure 1(c). In light of these simulations, it is reasonable to

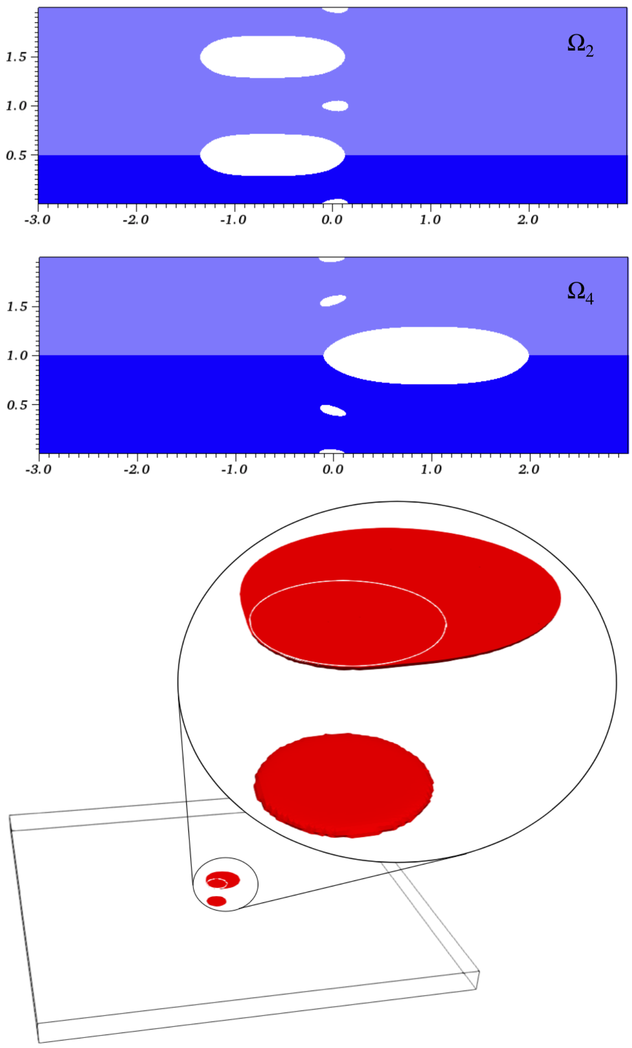

Fig. 5 (top,middle) 2D simulations. Fractured materials are removed for visualization purpose. The transparent regions correspond to mirrored domains using the symmetries. In all simulations only one of the crack tips propagates in one direction in the simulated domain. (bottom) Penny-shape crack propagation in a parallel network with $\delta = 2l_0$. The initial crack is indicated by a white line. Only one of the cracks propagates, breaking the rotational symmetry.

challenge the classical assumption of penny-shaped or bi-wing cracks under some conditions.

5 Discussion and conclusion

Problems in hydraulic fracturing are commonly quantified in terms of a non-dimensional toughness and a non-dimensional viscosity [17]. The stability analysis of a system of two cracks in [41], input power analysis in [6], and numerical simulations in [12, 18] suggested that in the toughness dominated regime, when viscous dissipation and fluid migration from the crack to the surrounding rock can be neglected, multiple symmetric hydraulic fractures do not grow simultaneously. Indeed, it is a common industry practice to employ *limited entry* techniques to restrict the inflow in each crack [7, 26]. By introducing additional viscous dissipation, this approach is thought to contribute to an even distribution of fluid in cracks.

Our analysis and numerical simulations are consistent with the literature and empirical evidences. We show that in the toughness-dominated regime, a single crack propagating is *the most stable configuration*. In the case of closely packed initial cracks, we also show that *asymmetric propagation is energetically favored*. In all cases, the asymptotic formulas [33, 34] are a good approximation of the critical pressure upon which cracks will propagate but cannot predict the pressure drop during crack propagation as the configuration consisting of a single crack propagating is also associated with the highest injection pressure drop. Furthermore, the unstable nature of the propagation of multiple hydraulic cracks is a consequence of the non-convexity of the energy driving fracture propagation. As such, it is not altered by adding in-situ stresses or pore pressure, so the fracture behavior will be identical in these situations.

Note that this behavior should not come up as a surprise. The problem of two hydraulic cracks is also essentially similar to the classical experiment in which two connected balloons are pressurized but only one inflates [38] with the added complexity of the crack growth hypothesis.

Our findings challenge a common assumption in many computational models [39, 36, 25, 28, 11] and theoretical works [1]. While our analysis only applies to the toughness dominated regime, many systems, especially geothermal and carbon sequestration projects, fall within this regime because of the low fluid viscosity and the high fracture toughness.

6 Appendix

6.1 Propagation of a single hydraulic crack in an infinite domain

Here we discuss the closed form solutions of a pressurized straight crack in 2D and a penny-shape crack in 3D in more details. We start by recalling classical results [33] that provide an upper bound on the critical propagation pressure in two space dimensions (2D) followed by three dimensions (3D).

For 2D, the normal displacement on the crack is given by [33, 34]:

$$u_y(x, 0^{\pm}) = \pm \frac{2p}{E'} \sqrt{l_0^2 - x^2},$$

and the pressurized crack forms an elliptical cavity of volume

$$V := \frac{\mathcal{W}_p(l_0)}{p},$$

in the deformed configuration. The work of the pressure force is

$$\mathcal{W}_p(l_0) = \frac{2\pi p^2}{E'} l_0^2.$$

Owing to Clapeyron's theorem, the elastic energy is given by

$$\mathcal{E}_p(l_0) = -\frac{\pi p^2 l_0^2}{E'},$$

and the elastic energy release rate *with respect to a pressure change*, assuming propagation along the x-axis, is

$$G_p(l_0) := -\frac{1}{2}\frac{\partial \mathcal{E}_p}{\partial l}(l_0) = \frac{\pi p^2 l_0}{E'}.$$

Assuming a quasi-static evolution driven by an increasing injection pressure, stability in the sense of Griffith criterion $G_p \leq G_{\mathrm{c}}$ is satisfied as long as $p \leq p_0$ with

$$p_0 := \left(\frac{G_{\mathrm{c}} E'}{\pi l_0}\right)^{1/2},$$

and the volume of the cavity in the deformed configuration is

$$V_0 := 2\left(\frac{\pi G_{\mathrm{c}} l_0^3}{E'}\right)^{1/2}. \tag{4}$$

Note that p_0 is a decreasing function of l_0 so that once the injection pressure attains the critical value p_0, Griffith stability can no longer be attained.

When the driving parameter is the volume of the fracture in the deformed configuration (or injected fluid volume, assuming that the pressure force is achieved by injecting an incompressible fluid), the situation is different. The elastic energy becomes

$$\mathcal{E}_V(l_0) := \frac{E' V^2}{4\pi l_0^2},$$

and the elastic energy release rate *with respect to a volume change* is

$$G_V(l_0) = -\frac{1}{2}\frac{\mathrm{d}\mathcal{E}_V}{\mathrm{d}l_0}(l_0) = \frac{E' V^2}{4\pi l_0^3}.$$

Griffith's stability for a crack of length l_0 is satisfied as long as $V \leq V_0$ given in 4. When V reaches V_0, the crack must grow while satisfying $G(V, l) = G_{\mathrm{c}}$, from which we derive that

$$p(V) = \left(\frac{2E' G_{\mathrm{c}}}{\pi V}\right)^{1/3},$$

and

$$l(V) = \left(\frac{E' V^2}{4\pi G_{\mathrm{c}}}\right)^{1/3},$$

i.e. recovering the classical scaling law for the pressure drop in a propagating hydraulic crack [15].

Note that the same analysis can be performed in 3D, assuming a penny-shaped crack throughout the evolution with initial radius R_0. In this case, the critical pressure and volumes are given by

$$p_0 := \left(\frac{\pi G_c E'}{4R_0}\right)^{1/2},$$

and

$$V_0 := \frac{8}{3}\left(\frac{\pi G_c R_0^5}{E'}\right)^{1/2},$$

As the critical volume is exceeded, the injection pressure and crack radius are given by

$$p(V) = \left(\frac{G_c^3 E'^2 \pi^3}{12V}\right)^{1/5},$$

and

$$R(V) = \left(\frac{9E'V^2}{64\pi G_c}\right)^{1/5}.$$

6.2 Verification simulation

Here we present the verification of our numerical model against the closed form solution of a single hydraulic fracture in 2D and 3D. All computations were performed with the `vDef` open-source implementation of the variational phase-field approach to fracture [2] in non-dimensional form[2].

All the geometric parameters are defined in an invariant geometry (a reflexion axis in 2D and a rotation in 3D) depicted in Figure 6. Note, however, that we computed the simulations in the full domain. We set up all the geometric and material parameters identically for both problems as summarized in Table 1. To simulate the infinite domain considered in the closed form solutions, we set the edge size of the computational domain to 100 times the initial crack length, and refined the mesh near the expected area of propagation of the crack as shown in Figure 6.

h	L	H	W	l_0	E	ν	G_c	ℓ
0.005	100	11h	75h	0.114	1	0	1	$3h$

Table 1 Parameters used for the simulation of a single fracture in 2D and 3D.

The initial phase-field function needs to be constructed carefully when performing simulations of crack re-nucleation [35]. To obtain a proper phase-field profile, we seeded an initial crack of length strictly less than l_0. We then applied a pressure field in the pre-existing crack and monitored its propagation until the length, estimated from the level line $\alpha = 0.8$, reached l_0.

[2] Taking advantage of the linearity of the problem, all the parameters are scaled for computational efficiency. We can scale them back by multiplying the computed displacement by $\sqrt{G_c/E}$ and the pressure by $\sqrt{G_c E}$ using the actual values of G_c and E. More details on the rescaling can be found in [12]

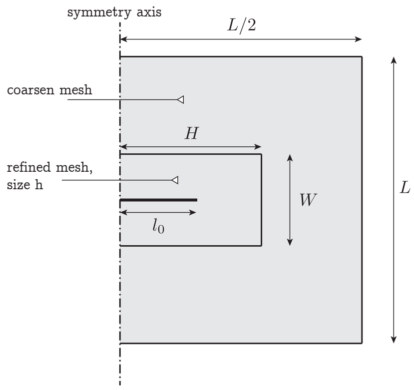

Fig. 6 Sketch of of the computational domain geometry. The symmetry axis being a reflection in 2D and a revolution axis in 3D.

Figure 7 shows snapshots of the evolution of the phase-field. The top figure represents the initial damage field obtained by enforcing $\alpha = 1$ on a one-element wide strip of length $< l_0$. The center figure shows the damage field associated with a crack of length l_0 obtained by pressurizing the initial crack. The lower figure shows the phase-field profile during the propagation phase. Notice the small difference between the phase profile near the crack tips in the first two figures.

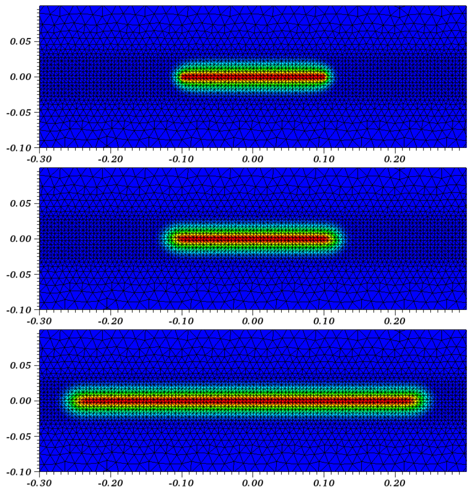

Fig. 7 Snapshots of phase-field profile for the line crack example at different loadings. Prior to the critical pressure loading (top), after the critical pressure loading (middle) and during the propagation (bottom). The red color represents fully damage material (fracture) and blue undamaged.

Figure 8 shows the crack in a 3D computation, by plotting the level surface $\alpha = 0.99$. Whereas the crack remains penny-shaped, it is not symmetrical with respect to the injection source. Such asymmetric growth has also been observed in laboratory experiments [9,8].

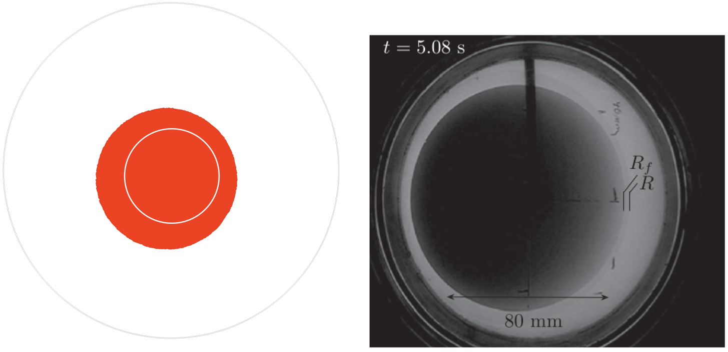

Fig. 8 A snapshot (view from above) of fracture damage ($\alpha \geq .99$) for the penny shape crack during the propagation (left). The solid white line indicates the initial crack and black line is the limit of the casing. An off–centered penny shape crack propagation was also observed in a toughness dominated hydraulic fracturing experiment as reported in [8] (right).

Figure 9 show the excellent agreement between crack radius and injection pressure from phase-field computations with the closed form solution in 2D and 3D. In both cases as long as the $V \leq V_c$ the crack does not grow and for $V > V_c$ the pressure starts to decline as $p \sim V^{-1/3}$ (line fracture) and $p \sim V^{-1/5}$ (penny-shape crack). Note that we have accounted for the "effective" toughness $(G_\mathrm{c})_\mathrm{eff} = G_\mathrm{c}\,(1 + 3h/8\ell\,)$ induced by the finite discretization size [5].

Acknowledgements Support for BB was provided in part by a grant from the U.S. National Science Foundation "Diffusion-driven fracture" DMS 1716763.

References

1. Bažant, Z.P., Salviato, M., Chau, V.T., Viswanathan, H., Zubelewicz, A.: Why fracking works. J. Appl. Mech. **81**(10), 101010–1 (2014). DOI 10.1115/1.4028192
2. Bourdin, B.: mef90/vDef: variational models of defect mechanics (2019). DOI 10.5281/zenodo.3242131. URL https://github.com/bourdin/mef90
3. Bourdin, B., Chukwudozie, C., Yoshioka, K.: A variational approach to the numerical simulation of hydraulic fracturing. In: Proceedings of the 2012 SPE Annual Technical Conference and Exhibition, vol. SPE 159154 (2012). DOI 10.2118/159154-MS
4. Bourdin, B., Francfort, G., Marigo, J.J.: Numerical experiments in revisited brittle fracture. J. Mech. Phys. Solids **48**(4), 797–826 (2000). DOI 10.1016/S0022-5096(99)00028-9
5. Bourdin, B., Francfort, G., Marigo, J.J.: The variational approach to fracture. J. Elasticity **91**(1-3), 1–148 (2008). DOI 10.1007/s10659-007-9107-3
6. Bunger, A.: Analysis of the power input needed to propagate multiple hydraulic fractures. Int. J. Solids Structures **50**(10), 1538–1549 (2013). DOI 10.1016/j.ijsolstr.2013.01.004
7. Bunger, A., Jeffrey, R.G., Zhang, X.: Constraints on simultaneous growth of hydraulic fractures from multiple perforation clusters in horizontal wells. SPE J. **19**(04), 608–620 (2014). DOI 10.2118/163860-PA
8. Bunger, A.P., Gordeliy, E., Detournay, E.: Comparison between laboratory experiments and coupled simulations of saucer-shaped hydraulic fractures in homogeneous brittle-elastic solids. J. Mech. Phys. Solids **61**(7), 1636–1654 (2013). DOI 10.1016/j.jmps.2013.01.005

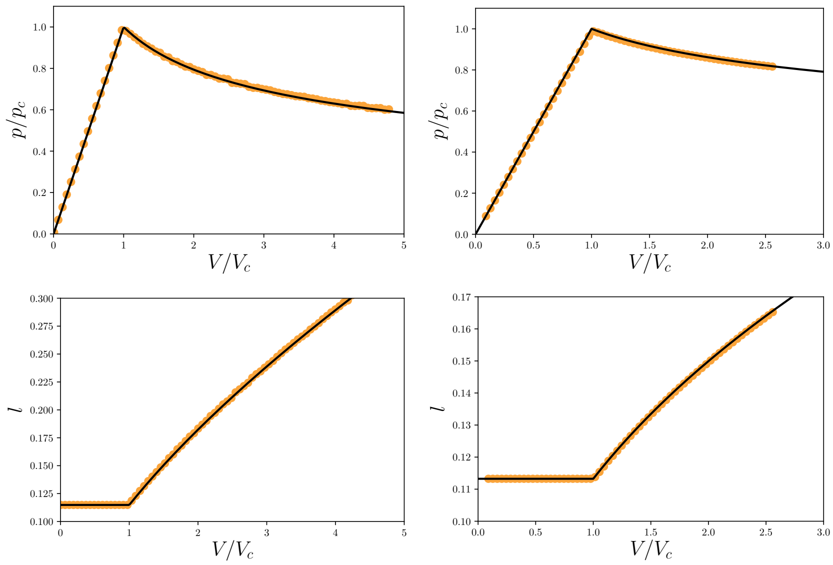

Fig. 9 Evolutions of normalized p, V and l for the line fracture (left column figures) and penny shape crack (right column figures). Colored dots refer to numerical results and solid black lines to the closed form solution given in Section 6.1.

9. Bunger, A.P., Jeffrey, R.G., Detournay, E.: Evolution and morphology of saucer-shaped sills in analogue experiments. In: Structure and Emplacement of High-Level Magmatic Systems, pp. 109–120. Geological Society, London (2008). DOI 10.1144/SP302.8
10. Castonguay, S.T., Mear, M.E., Dean, R.H., Schmidt, J.H., et al.: Predictions of the growth of multiple interacting hydraulic fractures in three dimensions. In: SPE annual technical conference and exhibition. Society of Petroleum Engineers (2013)
11. Chen, X., Zhao, J., Li, Y., Yan, W., Zhang, X.: Numerical simulation of simultaneous hydraulic fracture growth within a rock layer: Implications for stimulation of low-permeability reservoirs. J. Geophys. Res.-Sol. Ea. **124**(12), 13227–13249 (2019). DOI 10.1029/2019JB017942
12. Chukwudozie, C., Bourdin, B., Yoshioka, K.: A variational phase-field model for hydraulic fracturing in porous media. Comp. Meth. Appl. Mech. Engng. **347**, 957–982 (2019). DOI 10.1016/j.cma.2018.12.037
13. Cramer, D., Friehauf, K., Roberts, G., Whittaker, J., et al.: Integrating DAS, treatment pressure analysis and video-based perforation imaging to evaluate limited entry treatment effectiveness. In: SPE Hydraulic Fracturing Technology Conference and Exhibition. Society of Petroleum Engineers (2019). DOI 10.2118/194334-MS
14. Dahi-Taleghani, A., Olson, J.E.: Numerical modeling of multistranded-hydraulic-fracture propagation: Accounting for the interaction between induced and natural fractures. SPE J. **16**(3), 575–581 (2011). DOI 10.2118/124884-PA
15. Dean, R.H., Schmidt, J.H.: Hydraulic-fracture predictions with a fully coupled geomechanical reservoir simulator. SPE J. **14**(December), 707–714 (2009). DOI 10.2118/116470-PA
16. Detournay, E.: Mechanics of hydraulic fractures. Annual Review of Fluid Mechanics **48**(1), 311–339 (2016). DOI 10.1146/annurev-fluid-010814-014736
17. Detournay, E., Garagash, D.I.: The near-tip region of a fluid-driven fracture propagating in a permeable elastic solid. J. Fluid Mech. **494**, 1–32 (2003). DOI 10.1017/S0022112003005275
18. Dontsov, E., Suarez-Rivera, R.: Propagation of multiple hydraulic fractures in different regimes. Int. J. Rock Mech. Min. **128**, 104270 (2020). DOI 10.1016/j.ijrmms.2020.104270
19. Fischer, T., Hainzl, S., Eisner, L., Shapiro, S.A., Le Calvez, J.: Microseismic signatures of hydraulic fracture growth in sediment formations: Observations and modeling. J. Geophys. Res.-Sol. Ea. **113**(2), 1–12 (2008). DOI 10.1029/2007JB005070

20. Francfort, G., Marigo, J.J.: Revisiting brittle fracture as an energy minimization problem. J. Mech. Phys. Solids. **46**(8), 1319–1342 (1998). DOI 10.1016/S0022-5096(98)00034-9
21. Gao, H., Rice, J.R.: Somewhat circular tensile cracks. Int. J. Fracture **33**(3), 155–174 (1987). DOI 10.1007/BF00013168
22. Gordeliy, E., Abbas, S., Peirce, A.: Modeling nonplanar hydraulic fracture propagation using the XFEM: An implicit level-set algorithm and fracture tip asymptotics. Int. Jo. Solids Struct. **159**, 135–155 (2019). DOI 10.1016/j.ijsolstr.2018.09.025
23. Griffith, A.A.: The phenomena of rupture and flow in solids. Philos. T. R. Soc. S-A **221**, 163–198 (1921). DOI 10.1098/rsta.1921.0006
24. Kresse, O., Weng, X.: Numerical modeling of 3d hydraulic fractures interaction in complex naturally fractured formations. Rock Mech. Rock Eng. **51**(12), 3863–3881 (2018). DOI 10.1007/s00603-018-1539-5
25. Kresse, O., Weng, X., Gu, H., Wu, R.: Numerical modeling of hydraulic fractures interaction in complex naturally fractured formations. Rock Mech. Rock Eng. **46**(3), 555–568 (2013). DOI 10.1007/s00603-012-0359-2
26. Lecampion, B., Desroches, J.: Simultaneous initiation and growth of multiple radial hydraulic fractures from a horizontal wellbore. J. Mech. Phys. Solids **82**, 235–258 (2015). DOI 10.1016/j.jmps.2015.05.010
27. Marigo, J.J., Maurini, C., Pham, K.: An overview of the modelling of fracture by gradient damage models. Meccanica **51**(12), 3107–3128 (2016). DOI 10.1007/s11012-016-0538-4
28. McClure M., W., Mohsen, B., Sogo, S., Jian, H.: Fully coupled hydromechanical simulation of hydraulic fracturing in 3D discrete-fracture networks. SPE Journal **21**(4), 1302–1320 (2016). DOI 10.2118/173354-PA
29. Meyer, C.: Matrix Analysis and Applied Linear Algebra. SIAM (2000)
30. Murakami, Y., et al.: Handbook of stress intensity factors. Pergamon Press, Oxford (UK). (1987)
31. Pham, K., Amor, H., Marigo, J.J., Maurini, C.: Gradient damage models and their use to approximate brittle fracture. Int. J. Damage Mech. **20**(4, SI), 618–652 (2011). DOI 10.1177/1056789510386852
32. Shauer, N., Duarte, C.A.: Improved algorithms for generalized finite element simulations of three-dimensional hydraulic fracture propagation. Int. J. Numer. Anal. Met. **43**(18), 2707–2742 (2019). DOI 10.1002/nag.2977
33. Sneddon, I., Elliott, H.: The opening of a Griffith crack under internal pressure. Q. Appl. Math. **4**(262) (1946). DOI 10.1090/QAM/17161
34. Sneddon, I., Lowengrub, M.: Crack problems in the classical theory of elasticity. John Wiley & Sons (1969)
35. Tanné, E., Li, T., Bourdin, B., Marigo, J.J., Maurini, C.: Crack nucleation in variational phase-field models of brittle fracture. J. Mech. Phys. Solids **110**, 80–99 (2018). DOI 10.1016/j.jmps.2017.09.006
36. Wang, H.Y.: Poro-elasto-plastic modeling of complex hydraulic fracture propagation: simultaneous multi-fracturing and producing well interference. Acta Mech. **227**(2), 507–525 (2016). DOI 10.1007/s00707-015-1455-7
37. Warpinski, N., Teufel, L.: Influence of geologic discontinuities on hydraulic fracture propagation. J. Petrol. Technol. **39**(02), 209–220 (1987). DOI 10.2118/13224-PA
38. Weinhaus, F., Barker, W.: On the equilibrium states of interconnected bubbles or balloons. Am. J. Phys. **46**(10), 978–982 (1978). DOI 10.1119/1.11487
39. Wu, K., Olson, J., Balhoff, M.T., Yu, W.: Numerical analysis for promoting uniform development of simultaneous multiple-fracture propagation in horizontal wells. SPE Prod. & Oper. **32**(1), 41–50 (2016). DOI 10.2118/174869-PA
40. Yamamoto, K., Shimamoto, T., Sukemura, S.: Multiple fracture propagation model for a three-dimensional hydraulic fracturing simulator. Int. J. Geomech. **4**(1), 46–57 (2004). DOI 10.1061/(ASCE)1532-3641(2004)4:1(46)
41. Zeng, Q., Liu, Z., Wang, T., Gao, Y., Zhuang, Z.: Stability analysis of the propagation of periodic parallel hydraulic fractures. Int. J. Fracture **208**(1-2), 191–201 (2017). DOI 10.1007/s10704-017-0233-z
42. Zhang, X., Jeffrey, R.G., Thiercelin, M.: Mechanics of fluid-driven fracture growth in naturally fractured reservoirs with simple network geometries. J. Geophys. Res.-Sol. Ea. **114**(B12) (2009). DOI 10.1029/2019JB017942